Received February 2001
Revised May 2001
Accepted May 2001

Three-dimensional computational modelling of momentum, heat and mass transfer in laser surface alloying with distributed melting of alloying element

P. Mohan Raj and S. Sarkar
Department of Mechanical Engineering, Indian Institute of Science, Bangalore, India
S. Chakraborty
Department of Power Plant Engineering, Jadavpur University, Calcutta, India, and
P. Dutta
Department of Mechanical Engineering, Indian Institute of Science, Bangalore, India

Keywords *Heat transfer, Alloys, Modelling*

Abstract *A transient, three-dimensional mathematical model of a single-pass laser surface alloying process has been developed to examine the macroscopic heat, momentum and species transport during the process. A numerical study is performed in a co-ordinate system moving with the laser at a constant scanning speed. A fixed grid enthalpy-porosity approach is used, which predicts the evolutionary development of the laser-melted pool. It is observed that the melting of the added alloying element is not instantaneous in case its melting temperature is higher as compared to that of the base metal. As a result, the addition of alloying element at the top surface cannot be accurately modelled as a mass flux boundary condition at that surface. To resolve this situation, the addition of alloying elements is formulated by devising a species generation term for the solute transport equation. By employing a particle-tracking algorithm and a simultaneous particle-melting consideration, the species source term is estimated by the amount of fusion of a spherical particle as it passes through a particular control volume. Numerical simulations are performed for Ni as alloying element on Al base metal. It is revealed that the present model makes a distinctly different prediction of composition variation within the resolidified microstructure, as compared to a model that does not incorporate any considerations of distributed melting.*

Nomenclature

a_P, a_P^0 = discretisation equation coefficients
b = small number to avoid division by zero
c = specific heat
D = species mass diffusion coefficient
f_l = liquid fraction of the solute
F^{-1} = inverse of latent heat function
g = acceleration due to gravity
h = convective heat transfer coefficient
h_s = sensible enthalpy
H = total enthalpy
k = thermal conductivity

International Journal of Numerical Methods for Heat & Fluid Flow, Vol. 11 No. 6, 2001, pp. 576-599.

k_p = partition coefficient
K = morphological constant
L = latent heat of fusion
m_f = powder feed rate
$\dot{m}$ = mass flux
n = normal direction
P = pressure
q'' = heat flux
Q = actual power input
r_q = radius of heat input
R = reference width of the pool
$\overline{R}$ = universal gas constant
S = source term
T = temperature
t = time
u = x-component of velocity
u_{scan} = laser scanning velocity
v = y-component of velocity
v_n = interface velocity
w = z-component of velocity
x' = x-coordinate in a fixed frame of reference
x,y,z = co-ordinates fixed to the laser source

Greek symbols
β_T = coefficient of volumetric expansion of heat
β_C = coefficient of volumetric expansion of solute
η = efficiency
Γ = diffusion coefficient in general transport equation
ΔH = latent enthalpy
ε = emissivity
ϕ = general scalar variable
λ = relaxation factor
σ = surface tension
σ_T = surface tension coefficient of temperature
σ_e = Stefan-Boltzman constant
ρ = density
μ = viscosity

Subscripts
Al = aluminium
Fe = iron
max = maximum value
m = melting point
n = iteration level/normal direction
old = old iteration value
p = nodal coefficient
ref = reference

Superscripts
/ = stationary co-ordinate system

Introduction

Surface properties such as wear and corrosion resistance are governed by a thin layer of material in a localized area over the surface. Laser surface alloying (LSA) is one such technique where, without changing the bulk properties of a component, material properties can be improved in a localized region. During this process, as the high- intensity moving laser heat source interacts with a thin molten layer of the substrate, several complex phenomena such as melting, Marangoni convection, mixing of the powder feed, alloy solidification and resulting micro-structural evolution occur. Looking into the complexity of the problem, our aim is to develop systematically a reliable computational model that can simulate the entire physical process which includes heating and subsequent melting of the substrate due to a moving heat source, surface-tension driven convection, mixing of the added species and solidification of the molten material. The model may be used to link the process parameters for the prediction of final microstructure.

Numerical studies of heat transfer and fluid flow in laser melted pools have been performed by several researchers in the past (Chan *et al.*, 1984, 1987, 1988; Basu and Srinivasan, 1988; Kou and Wang, 1986; Chen and Huang, 1990; He *et al.*, 1995), mostly employing two-dimensional or axi-symmetric models. From the above studies, good insights have been obtained on the behaviour of laser melted pools subjected to various process parameters. Only a few studies

(notably that of He *et al.* (1995)) are on laser surface alloying, in which mass transfer is taken into account in addition to heat transfer and fluid flow. He *et al.* (1995) presented a two-dimensional finite element model for a single-pass laser surface alloying of copper on aluminium base metal. The alloying element is assumed to be introduced on the pool surface in a fully molten state. This is modelled numerically as a mass flux boundary condition at the pool surface. This approximation holds reasonably well as long as the melting point of the substrate is much higher than that of the alloying element (such as in the case of aluminium on iron). This boundary condition, however, is generally inappropriate when the melting point of the alloying element is higher than that of the substrate (such as in the case of nickel on aluminium). In this situation, an alloying particle will melt only within that region of the pool where it experiences a temperature higher than its melting point. The particle, instead of melting completely on the pool surface, may melt progressively as it is convected within the pool, thus resulting in a distributed species mass source within the pool.

The aim of the present work is to model an LSA process with a distributed species mass source term. This involves modelling the melting of an alloying particle as it is convected within the pool. The molten mass at any location forms the species mass source at that location, which leads to a distributed species mass source in the melt pool. The necessary velocity and temperature fields are obtained by the solution of three-dimensional, transient mass, momentum and energy conservation equations. The numerical solution is obtained using a fixed-grid, primitive-variable, finite volume methodology with an enthalpy-porosity approach (Brent *et al.*, 1988) to treat melting and solidification. Finally, the species conservation equation is solved using the above velocity field and above distributed mass source. It may also be noted here that the present model is the first three-dimensional model in this application, which is a more realistic representation of the actual physical situation.

Mathematical and numerical modelling

Figure 1 shows a schematic diagram of a typical laser surface alloying process. As shown in the figure, a laser beam moving with a constant scanning speed in the horizontal direction and having a defined power distribution strikes the surface of an opaque material, and a part of the energy is absorbed. A thin melt pool forms on the surface due to laser heating. Simultaneously, a powder of a different material is fed into the pool, which mixes with the molten substrate by convection and diffusion. As the laser source moves away from a location, resolidification of the zone occurs, leading to a final microstructure of the alloyed surface. It should be noted that only a part of the heat available from the laser beam heats the surface of the workpiece and leads to the formation of a molten pool. Hence, in the thermal modelling of laser surface alloying, the actual power, q, that goes into the workpiece as heat input is usually specified

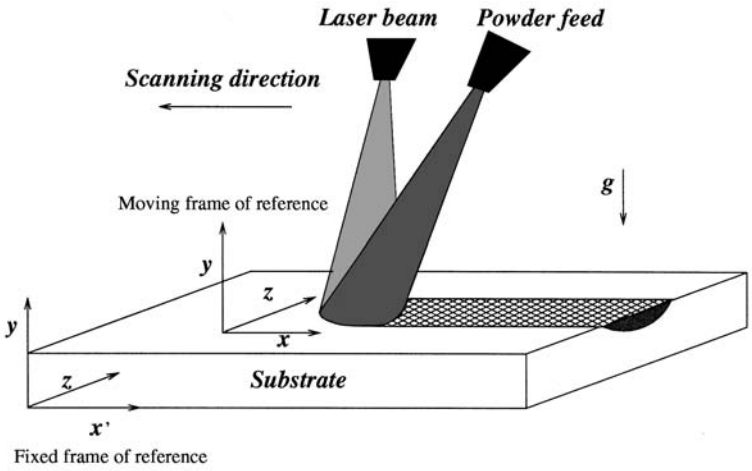

Figure 1.
A schematic diagram of the physical problem

through a parameter, η, the laser beam efficiency, by the relation $q = \eta Q$, where Q represents the total laser power.

Model description

The entire modelling is systematically divided into four modules. The first module consists of a solution of three-dimensional mass, momentum and energy conservation equations to obtain the velocity and temperature fields in and around the laser melted pool. This velocity field is used in the second module of the model, which involves tracking of alloying particles (in a Lagrangian frame) as it is advected within the pool. The third module simulates the progressive melting of each particle as it is advected within the pool, using the temperature field (obtained from the first part of the model) as a boundary temperature of the particle. As the melting particle is tracked, we record the amount of molten particle in each control volume along its trajectory. The same procedure is repeated for each particle, in order to obtain a statistical distribution of species mass source. Finally, in the fourth module, the species conservation equation is solved after each time-step using the above velocity field and distributed mass source. In this model, it is assumed that the alloying particles are spherical in shape and move without any relative velocity with the fluid particles. The details of the module descriptions are as follows.

Solution of the velocity and temperature fields (module 1). If (x′, y, z) is a co-ordinate system in the stationary frame, then the generalised convection-diffusion equation in that frame can be written as:

$$\frac{\partial}{\partial t}(\rho\phi) + \frac{\partial}{\partial x'}(\rho u\phi) + \frac{\partial}{\partial y}(\rho v\phi) + \frac{\partial}{\partial z}(\rho w\phi) = \frac{\partial}{\partial x'}\left(\Gamma\frac{\partial\phi}{\partial x'}\right) + \frac{\partial}{\partial y}\left(\Gamma\frac{\partial\phi}{\partial y}\right) + \frac{\partial}{\partial z}\left(\Gamma\frac{\partial\phi}{\partial z}\right) + S. \quad (1)$$

Since the molten pool moves with the laser beam, the problem is more conveniently studied in a reference frame fixed with the laser. Although a final quasi-steady state will be reached, we prefer to study it in a transient mode so as to predict the evolution of pool development. The final shape and size of the pool depends on this evolution, and hence it cannot be determined accurately by a direct quasi-steady formulation. If (x, y, z) is a Cartesian co-ordinate system fixed with the laser, the following transformation equations can be written:

$$x = x' - u_{scan}t, \tag{2}$$

where u_{scan} is the scanning speed of the laser. Differentiating equation (2) with respect to t and noting that u_{scan} is a constant, we get:

$$u = u' - u_{scan}. \tag{3}$$

Using the above transformation equations, the governing equations in the moving frame can be written as (Dutta *et al.*, 1995):

- *continuity equation*:

$$\frac{\partial}{\partial x}(\rho u) + \frac{\partial}{\partial y}(\rho v) + \frac{\partial}{\partial z}(\rho w) = 0, \tag{4}$$

- *x-momentum equation*:

$$\begin{aligned} \frac{\partial}{\partial t}(\rho u) + \frac{\partial}{\partial x}(\rho uu) + \frac{\partial}{\partial y}(\rho uv) + \frac{\partial}{\partial z}(\rho uw) = -\frac{\partial p}{\partial x} \\ + \frac{\partial}{\partial x}(\mu\frac{\partial u}{\partial x}) + \frac{\partial}{\partial y}(\mu\frac{\partial u}{\partial y}) + \frac{\partial}{\partial z}(\mu\frac{\partial u}{\partial z}) + S_x - \frac{\partial}{\partial x}(\rho u_{scan}u), \end{aligned} \tag{5}$$

- *y-momentum equation*:

$$\begin{aligned} \frac{\partial}{\partial t}(\rho v) + \frac{\partial}{\partial x}(\rho uv) + \frac{\partial}{\partial y}(\rho vv) + \frac{\partial}{\partial z}(\rho vw) = -\frac{\partial p}{\partial y} + \frac{\partial}{\partial x}(\mu\frac{\partial v}{\partial x}) \\ + \frac{\partial}{\partial y}(\mu\frac{\partial v}{\partial y}) + \frac{\partial}{\partial z}(\mu\frac{\partial v}{\partial z}) - \frac{\partial}{\partial x}(\rho u_{scan}v) + \rho g\beta_T(T - T_{ref}) \\ + \rho g\beta_C(C - C_{ref}) + S_y, \end{aligned} \tag{6}$$

- *z-momentum equation*:

$$\begin{aligned} \frac{\partial}{\partial t}(\rho w) + \frac{\partial}{\partial x}(\rho uw) + \frac{\partial}{\partial y}(\rho vw) + \frac{\partial}{\partial z}(\rho ww) = -\frac{\partial p}{\partial z} + \frac{\partial}{\partial x}(\mu\frac{\partial w}{\partial x}) \\ + \frac{\partial}{\partial y}(\mu\frac{\partial w}{\partial y}) + \frac{\partial}{\partial z}(\mu\frac{\partial w}{\partial z}) - \frac{\partial}{\partial x}(\rho u_{scan}w) + S_z, \end{aligned} \tag{7}$$

where S_x, S_y and S_z are source terms, which will be described subsequently; and

- *energy equation*:

$$\frac{\partial}{\partial t}(\rho H)+\frac{\partial}{\partial x}(\rho u H)+\frac{\partial}{\partial y}(\rho v H)+\frac{\partial}{\partial z}(\rho w H)=\frac{\partial}{\partial x}(k\frac{\partial T}{\partial x})+\frac{\partial}{\partial y}(k\frac{\partial T}{\partial y})+\frac{\partial}{\partial z}(k\frac{\partial T}{\partial z})-\frac{\partial}{\partial x}(\rho u_{scan}H). \tag{8}$$

The enthalpy, H, of a material can be expressed as:

$$H=h_s+\Delta H, \tag{9}$$

$$h_s=cT, \tag{10}$$

where h_s is the sensible heat, and ΔH is the latent heat content. In order to establish a mushy phase change, the latent heat contribution is specified as a function of temperature, T, and the resulting expression is:

$$\Delta H=f(T). \tag{11}$$

Since latent heat is associated with the liquid fraction, f_l, we can write:

$$\begin{aligned}\Delta H=f(T) &= L \quad for \quad T\geq T_l\\ &= f_l L \quad for \quad T_s\leq T<T_l\\ &= 0 \quad for \quad T<T_s,\end{aligned} \tag{12}$$

where T_l is the liquidus temperature at which solid formation begins, T_s is the solidus temperature at which full solidification occurs, and L is the latent heat of fusion. Substituting the expression for H from equations (9) and (10) in the energy equation (8), we arrive at the following final form of the energy equation:

$$\frac{\partial}{\partial t}(\rho T)+\frac{\partial}{\partial x}(\rho u T)+\frac{\partial}{\partial y}(\rho v T)+\frac{\partial}{\partial z}(\rho w T)=\frac{\partial}{\partial x}(\frac{k}{c}\frac{\partial T}{\partial x})+\frac{\partial}{\partial y}(\frac{k}{c}\frac{\partial T}{\partial y})+\frac{\partial}{\partial z}(\frac{k}{c}\frac{\partial T}{\partial z})-\frac{\partial}{\partial x}\left(\rho u_{scan}\left(T+\frac{\Delta H}{c}\right)\right)+S_e, \tag{13}$$

where S_e is the source term in the energy equation, which can be written as:

$$S_e=\frac{1}{c}\frac{\partial}{\partial t}(\rho\Delta H)-\nabla.\left(\frac{\rho}{c}\vec{u}\Delta H\right). \tag{14}$$

In the above formulation, a single-domain enthalpy-porosity model (Brent *et al.*, 1988) is used for the phase change process. In this method, the interface geometry and location come out as a part of the solution, and hence explicit

interface tracking is not required. The source terms in the three momentum equations (5)-(7) take the following forms:

$$S_x = Au, \tag{15}$$

$$S_y = Av, \tag{16}$$

$$S_z = Aw, \tag{17}$$

where the expression for A is given by the relation:

$$A = -\left(\frac{K(1-f_l)^2}{f_l^3 + b}\right). \tag{18}$$

In the above equation, K is a morphological constant of a high value (say, 10^8), b is a small number (say, 10^{-4}) to avoid division by zero and f_l is the liquid fraction calculated as $(\Delta H)/L$. The source term in each of the equations (5)-(7) represents a porous-medium-like resistance in the mushy region at the solid-liquid interface. In the fully liquid region, the value of f_l is 1, making the porous-medium-resistance terms zero. On the other hand, in the fully solid region, $f_l = 0$, thus forcing the porous medium resistance terms to be very large. These large source terms offer a high flow resistance, making the velocities in the entire solid region effectively zero. In the mushy region, however, f_l lies between 0 and 1, and the porous medium resistance varies smoothly from zero in the liquid region to a high value in the solid region, thus making the velocities vary accordingly.

For boundary conditions, at the top surface, we employ a heat balance as follows:

$$-q''(r) + h(T - T_\infty) + \sigma_e \varepsilon (T^4 - T_\infty^4) = -k\frac{\partial T}{\partial y}, \tag{19}$$

where $q''(r)$ is expressed as a Gaussian heat distribution at the top surface, i.e.:

$$q''(r) = \frac{Q}{\pi r_q^2} \exp\left(-\frac{r^2}{r_q^2}\right). \tag{20}$$

In the above equation, Q is the net energy input (*laser power* $\times$ *efficiency*) and r_q is the radius of heat input. The top surface is assumed to be flat. Also, at the top surface, the Marangoni convection leads to a shear stress balance expressed as:

$$\tau_{yx} = -\mu\left(\frac{\partial u}{\partial y}\right)_h = \frac{\partial \sigma}{\partial T}\left(\frac{\partial T}{\partial x}\right)_h, \tag{21}$$

$$\tau_{yz} = -\mu\left(\frac{\partial w}{\partial y}\right)_h = \frac{\partial \sigma}{\partial T}\left(\frac{\partial T}{\partial z}\right)_h, \tag{22}$$

where σ is the surface tension.

The four side faces are subjected to the convective heat transfer boundary condition:

$$-k\left(\frac{\partial T}{\partial n}\right)_{wall} = h(T - T_\infty), \tag{23}$$

where n is in the direction of the outward normal of any side face. The bottom face being insulated, the appropriate boundary condition is:

$$\left(\frac{\partial T}{\partial y}\right)_{bottom} = 0. \tag{24}$$

The three-dimensional governing equations of mass, momentum and energy conservation are simultaneously solved numerically using a pressure-based, semi-implicit finite volume technique according to the SIMPLER algorithm (Patankar, 1980). The algorithm is appropriately modified to include the enthalpy-porosity model for the phase change process. The porous-medium source terms in the momentum equations (5)-(7) are calculated for any control volume using the value of liquid fraction, f_l, for that particular control volume. The value of liquid fraction is calculated as $f_l = (\Delta H)/L$, where ΔH, the latent heat content of a particular control volume, is obtained from the solution of the energy conservation equation. In the numerical solution of the energy conservation equation, a special treatment is applied to update the nodal latent heat content. The procedure, which is elaborated in Brent *et al.* (1988) and Voller and Prakash (1987), is briefly described below. The enthalpy update is governed by the equation:

$$[\Delta H_p]_{n+1} = [\Delta H_p]_n + \frac{a_p}{a_p^0}\lambda\left\{[h_p]_n - F^{-1}(\Delta H)\right\}, \tag{25}$$

where n denotes the iteration level and λ is a relaxation factor. The terms a_p and a_p^0 are the nodal-point coefficient and the coefficient associated with the transient part in the discretised energy equation, respectively.

Particle tracking (module 2). The position and local temperature in the trajectory of an alloying particle (Lagrangian frame) introduced into the molten pool is calculated from the fully developed Eulerian velocity field obtained in module 1. It is assumed that the particle moves with the same velocity as that of the fluid at that location. The trajectory of the particle is governed by the following ordinary differential equations:

$$\frac{dx}{dt} = u(x, y, z, t'), \tag{26a}$$

$$\frac{dy}{dt} = v(x, y, z, t'), \tag{26b}$$

$$\frac{dz}{dt} = w(x, y, z, t'), \tag{26c}$$

where u, v and w are the velocity components in the three directions. These velocity components are numerically integrated in a time marching scheme using a fourth-order Runge-Kutta method to obtain the complete particle trajectory. It should be noted that, from module 1, the velocity components are specified only at the grid points. For all other locations, a tri-linear interpolation is performed using the velocities at the neighbouring grid points. Thus, the incremental positions are obtained in the three directions and the solution is marched with time to get the complete particle trajectory. Simultaneously, the local temperature is interpolated at each and every incremental location in the locus of the particle. This information will be necessary in the calculations pertaining to particle melting in module 3.

Particle melting (module 3). After introduction of an alloying particle into the melt pool, it is subjected to temperature boundary conditions in accordance with the local temperature of the pool. As the particle is advected within the pool, its temperature boundary condition also varies according to its location. The particle-melting module solves the transient temperature distribution within the particle (including melting) using a conduction-based analysis. Because of the radially symmetric temperature boundary condition, the heat transfer inside a spherical particle is assumed to be one-dimensional. The energy conservation equation for the particle in a spherical coordinate system is given by:

$$\frac{\partial}{\partial t}(\rho T) = \frac{1}{cr^2}\frac{\partial}{\partial r}(kr^2\frac{\partial T}{\partial r}) - \frac{1}{c}\frac{\partial}{\partial t}(\rho \Delta H). \tag{27}$$

Since the particle is moving in the melt pool, the surface temperature will vary with its location. This information can be obtained from module 2. Thus, during time marching, the interpolated local temperature in the melt pool for a particle location is used as the temperature boundary condition of the particle at that location. Accordingly, equation (27) is solved using the following boundary conditions:

$$\text{At } r = 0, \frac{\partial T}{\partial r} = 0 \text{ and at } r = r_p(t'), T_b(t') = T(x, y, z, t'), \tag{28}$$

where $r_p(t')$ and $T_b(t')$ are the radius and surface temperature of the particle, respectively, at the specified time t' in the Lagrangian frame. $T(x, y, z, t')$ is the interpolated local temperature (obtained from module 2) in accordance with the current location of the particle in the melt pool.

Since no analytical solution is available for the case of a melting spherical particle with a time-dependent boundary condition, a numerical solution is adopted. A control volume based finite difference method (Patankar, 1980) is used to formulate the 1D enthalpy-based energy equation of a melting spherical particle, in order to solve the temperature field within the same.

Species distribution (module 4). As the melting particle is tracked, the amount of molten particle in each control volume along its trajectory is recorded. This procedure is repeated for each and every particle introduced on the pool surface at various locations. Eventually, a statistical distribution of species mass source inside the pool can be obtained. Using the species mass source distribution, the following modified solute transport equation is obtained:

$$\frac{\partial}{\partial t}(\rho C_l) + \frac{\partial}{\partial x}(\rho u C_l) + \frac{\partial}{\partial y}(\rho v C_l) + \frac{\partial}{\partial z}(\rho w C_l) = \nabla.(\rho_l f_l D_l \nabla C_l) + k_p C_l \frac{\partial}{\partial t}(\rho f_l) - \frac{\partial}{\partial x}(\rho u_{scan} C_l) + k_p C_l \frac{\partial}{\partial x}(\rho u_{scan} f_l) + S_{gen}, \tag{29}$$

where S_{gen} represents a local volumetric species generation term. S_{gen} is calculated by the relation:

$$S_{gen} = \frac{\dot{m}_{cv}}{\Delta V}, \tag{30}$$

where $\dot{m}_{cv}$ is the rate at which the species mass melts in a control volume (statistical average for all particles) and ΔV is the volume of the particular computational cell. It can be noted that $\dot{m}_{cv}$ is obtained as a consequence of particle tracking and particle melting modules of the present model, in accordance with the local temperature distribution within the particle. Also, it is evident that S_{gen} is not active at all locations in the computational domain. In fact, it is active only at the control volumes where the particles melt. Hence, the above formulation of the species source term is a more realistic model of distributed melting than the specification of a mass flux boundary condition at the free surface, as used in previous studies.

The boundary conditions consistent with equation (29) at the interfaces are given by:

- *melting front*:

$$v_n C_l = -D_l \frac{\partial C_l}{\partial n}, \tag{31}$$

where v_n is the projection of the traverse speed onto the normal to the solid-liquid boundary; and

- *solidification front*:

$$(1 - k_p)v_n C_l = -D_l \frac{\partial C_l}{\partial n}. \tag{32}$$

The above modified species conservation equation is then solved numerically using a finite volume methodology (Patankar, 1980).

Numerical simulation

Code validation. The numerical code pertaining to the solution of a three-dimensional set of coupled convection-diffusion equations incorporating phase change considerations is validated by solving a Marangoni-convection driven arc welding problem, as described in Dutta *et al.* (1995). The results in Dutta *et al.* (1995) for the case of arc welding are exactly reproduced using the present code, and hence a separate figure for comparison is not included here. The computer code for the particle-melting module is validated against an analytical solution given in Carslaw and Jaeger (1959) corresponding to a fixed surface temperature. The validated codes are subsequently utilised for the solution of the present problem.

Choice of grid size and time step for module 1. In laser surface alloying, the presence of an intense heat flux leads to large temperature gradients in the base metal near the laser centre. This also induces rapid melting of the metal (typically in milliseconds) just after the laser is applied. As a result, choice of grid size and its distribution, along with the time steps for computation, are of paramount importance for numerical stability and accurate predictions of fluid flow and heat transfer in the pool.

At the top surface of the pool, viscous shear forces according to equations (21) and (22) balance surface tension forces caused by the temperature gradients. In order to resolve the velocity field at the free surface, the vertical gridding at these locations is ascertained by a scaling analysis, estimating the viscous boundary layer thickness created by surface tension driven flow. Such an estimate of boundary layer thickness (y_{ref}) is given by (Sarkar *et al.*, 2001):

$$y_{ref} \sim \left(\frac{\mu r_q}{\rho u_{ref}}\right)^{\frac{1}{2}}, \tag{33a}$$

where:

$$u_{ref} \sim \left(\frac{\sigma_T q}{\rho \mu c_p}\right). \tag{33b}$$

According to the physical properties depicted in Table I, it turns out to be 9×10^{-6}m. Accordingly, in order to resolve the velocity boundary layer computationally, six control volumes are accommodated within that distance in the vertical direction. Just beneath this fine grid system, a grid size of 5×10^{-5}m is used up to the bottom of the pool. In the horizontal planes, various grid sizes are tried,

	Values
Physical properties (constants)	
β_T (for aluminium)	2.0×10^{-5} K^{-1}
T_m (for aluminium)	660.0C
T_m (for nickel)	1,452.0C
T_{boil} (for aluminium)	2,520.0C
L (for aluminium)	3.95420×10^5J/kg
L (for nickel)	5.9×10^5J/kg
ρ (for aluminium)	2,237kg/m^3
ρ (for nickel)	8,890kg/m^3
σ_T (for aluminium)	-3.5×10^{-4}N/mK
Physical properties (variables)	
μ (for aluminium)	1.492×10^{-4} exp(16,500/$\overline{R}T$) Nm/s^2
k (for aluminium)	
$273K \leq T \leq 373K$	238.0W/mK
$373K \leq T \leq 993K$	231.4W/mK
$T \leq 993K$	109.3W/mK
k (for nickel)	74.9W/mK
c (for aluminium)	
$273K \leq T \leq 373K$	971J/kgK
$373K \leq T \leq 993K$	1049.2J/kgK
$T \leq 993K$	1212.0J/kgK
c (for aluminium)	441J/kgK

Table I.
List of physical properties

and it is found that a grid size of 6×10^{-5}m within the molten pool and its vicinity is adequately fine, because a finer grid system is not found to alter the results appreciably. Outside the pool in the solid region, a non-uniform coarser grid system is used. Overall, a $55 \times 40 \times 55$ non-uniform grid is chosen within a domain size of 10mm $\times$ 5mm $\times$ 10mm.

The time steps for computation are varied according to the stages of the melting process. During the pre-melting conduction phase, large time steps are used. But to take advantage of this, one needs to have an approximate estimate of time for initiation (t_{ref}) of melting before starting computation. This can be estimated as follows (Sarkar *et al.*, 2001):

$$t_{ref} \sim \rho c_p k \left(\frac{\Delta T}{q}\right)^2, \tag{34a}$$

where:

$$\Delta T \sim \frac{\mu u_{ref} r_q}{y_{ref} \sigma_T}. \tag{34b}$$

For the present set of problem data, t_{ref} comes to be approximately 0.01s. Accordingly, during the conduction phase, large time steps (about 0.005s) are allowed until melting begins. Once melting starts, the high temperature gradient in the pool sets up a strong Marangoni convection, leading to high

fluid velocities of the order of 1m/s. Hence, to avoid numerical oscillations, time steps during the initial stages of pool development are chosen to be very small (about 0.0005s). Typically after about 0.4s, the molten pool reaches a more developed stage, the implication of which is that changes in the dependent variables between two consecutive time steps are relatively small compared to those during the initial transients. At this stage, larger time steps (about 0.001s) can be safely used in order to save computation time. After 1s, the pool virtually reaches a fully developed state and at this stage time steps as high as 0.005s can be used without any numerical oscillation. Finally, to ensure that the fully developed stage has reached completely, computation is carried up to 1.5s.

Choice of grid size and time step for modules 2 and 3. Regarding the particle-melting module, a grid size of 202×1 is used for a particle size of 35μm radius to capture the interface movement accurately.

For the case of particle tracking, the error involved in the numerical integration with time marching must be reduced such that the trajectory of the particle is predicted accurately. Since the incremental position obtained in the first time step is going to be the initial condition for the next time step, the error associated in the first integration will propagate in the next time step, thereby leading to an erroneous species source term. Since the error associated with the numerical integration is a function of the time-step chosen, it is important to choose a sufficiently small time step for integration. Besides, there is a second criterion for choosing the time step. The assumption made in the species source addition is that for the entire time step, the mass molten (and hence the species source added) is at the same initial location as at the beginning of the time step. Hence, the time step is chosen in such a way that the particles do not skip any control volume during the integration. This is ensured by scaling the time step (Δt) as: $\Delta t \sim \Delta x/u_{\max}$, where Δx is the distance between two grid points. Based on the above two criteria, it is found that a time-step of 2.5×10^{-6}s is a suitable one and is used for both modules 2 and 3.

Convergence criteria. Convergence is declared if the following condition is satisfied at each grid point:

$$\left|\frac{\phi - \phi_{old}}{\phi_{\max}}\right| \leq 10^{-4}, \tag{35}$$

where ϕ stands for each variable (u, v, w, T and C) at a grid point at the current iteration level, ϕ_{old} represents a value at the previous iteration level, and $\phi_{\max}$ is the maximum value of the variable at that iteration level in the entire domain. Besides, an overall energy balance is performed during each time step, and the iterations are carried out until the absolute value of the energy balance is within 0.1 per cent of total energy input.

Results and discussion

Numerical simulations are carried out with Ni as alloying element and Al as the base metal. The thermo-physical properties, shown in Table I, are assumed to

be functions of temperature and composition, and are taken from Brandes (1983). The process parameters appropriate for the simulated problem are listed in Table II.

In order to validate the distributed melting approach, it is first applied to the case of laser surface alloying of aluminium on iron base metal (which represents the use of a lower melting-point alloy with a higher melting-point base metal). As a separate approach, numerical computations are also executed considering the mass flux of aluminium at the top surface to be in a completely molten state. The Neumann boundary condition (at the top surface) for the latter case can be written as:

$$-\left(D\frac{\partial C}{\partial y}\right)_{top} = \dot{m}, \tag{36}$$

where $\dot{m}$ is the mass flux of aluminium distributed uniformly over a circular area of radius r_q. In equation (36), D is the diffusion coefficient of the alloying element in the molten base material. The mass flux $\dot{m}$ is assumed to be uniform and is calculated from the powder feed rate (m_f) as:

$$\dot{m} = \left(\frac{m_f}{\pi r_q^2}\right). \tag{37}$$

It can be noted that the assumption of mass flux boundary condition at the top surface (i.e. equivalently, an instantaneous melting of the alloying element) is appropriate in this case, since the melting point of aluminium is much lower than that of iron. A comparison is made between the solidified interface composition obtained from the two procedures (with and without distributed melting approach), and is shown in Figure 2. The two results show excellent agreement, thus validating the procedure used for the distributed melting approach, which we use for the present formulation.

Nature of flow and temperature fields in the melt pool

Figures 3 and 4 show the velocity and temperature fields in three different views. A loop of very high velocity is found to exist immediately adjacent to the top surface of the pool. This flow is induced by the surface tension gradient (Marangoni convection) at the surface of the pool. It may be noted that this

Process parameters	Values
Q (total heat input)	2,400W
r_q (radius of heat input)	0.8mm
Radius of nickel particles	35×10^{-6}m
m_f (mass flux added)	2×10^{-5}kg/s
η (efficiency of heat input)	0.22
u_{scan} (laser scanning speed)	0.008m/s

Table II. List of process parameters

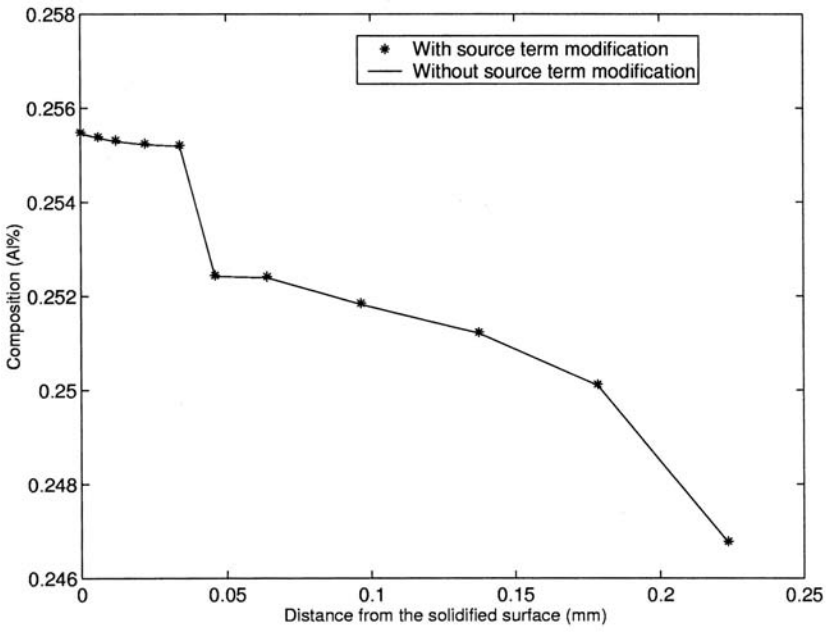

Figure 2.
Comparison of the solidified interface composition variation with height, with and without source term modification for the case of aluminium on iron for the parameters u_{scan} = 0.008m/s, *power* = 2.4kW, η = 0.13, and *powderfeed* = 0.02gm/s

turning effect of the fluid can be captured numerically, provided grid sizes near the top surface are made fine enough, according to the criterion discussed in the previous section. For the present case, the surface tension is a decreasing function of temperature. As a result, liquid metal near the centre of the pool is pulled towards the relatively cooler pool edges, resulting in counter-rotating vortices as shown in Figure 3. After the hot liquid metal from the pool centre reaches the edge, it turns downwards. It may be noted from Figure 3 that the weld pool geometry closely resembles that predicted by conduction analysis alone. The reason is that liquid aluminium has a low Prandtl number ($Pr \approx 0.004$), and hence the role of convection in the overall transport is not very significant. As a result, convection in the pool does not alter the pool geometry significantly, unlike the case of an iron substrate which has a higher Prandtl number. The resulting Peclet number ($u_{max} \times depth/(\alpha)$ for the case of aluminium is also found to be less ($Pe \approx 61$) compared to that of iron.

Behaviour of particles and the species distribution in the melt pool

In the temperature field shown in Figure 4, there are two regions which are of importance in determining the nature of species distribution in the melt pool. The first region is the zone where the temperatures are higher than the melting point of the alloying element, nickel (1,452°C). The other region is the zone where the temperatures are lower than the melting point of the alloying element but above the melting point of the base metal, aluminium (660°C). These two regions are shown in Figure 4. In a three-dimensional picture, these two regions resemble two stretched hemispheres or cups. The stretching is due to the effect

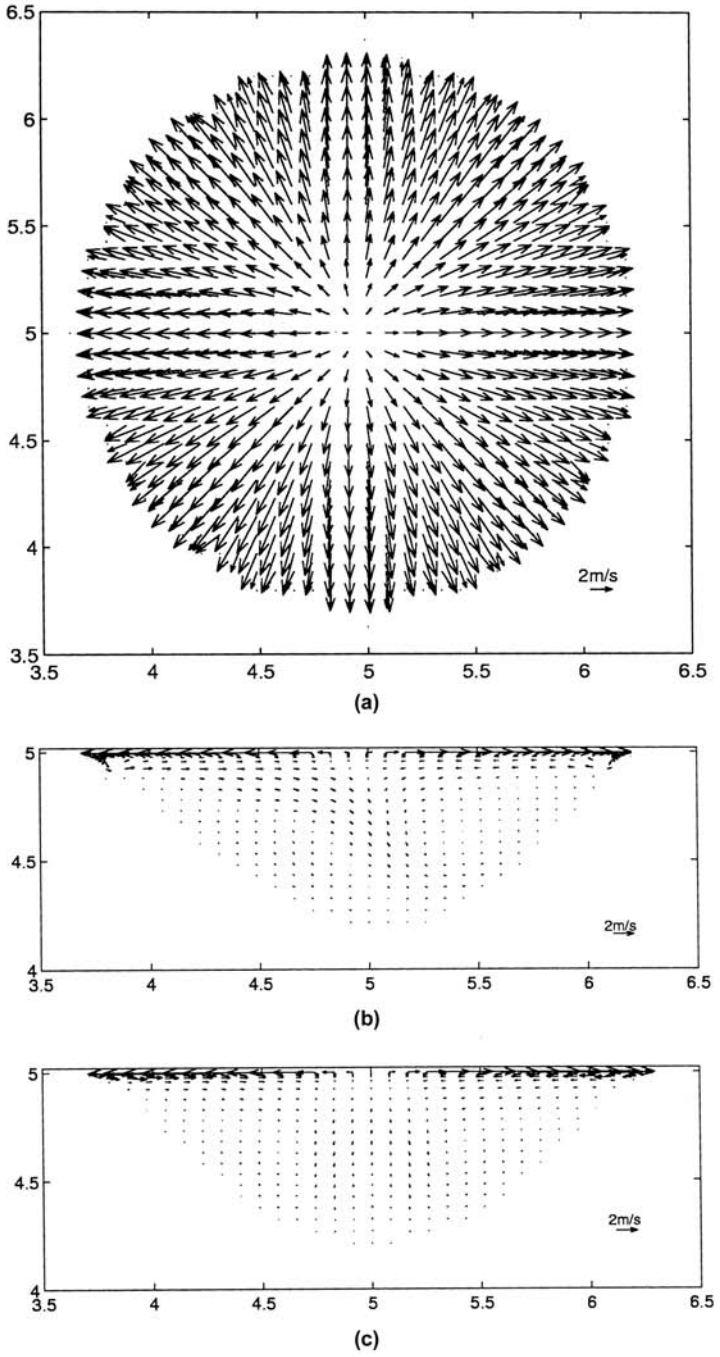

Note: (a) top view, (b) longitudinal sectional view along the laser centre line and (c) cross sectional view in the plane of the laser.
All dimensions are in mm

Figure 3.
Velocity vector plot for the case of u_{scan} = 0.008m/s, *power* = 2.4kW, η = 0.22, and *powderfeed* = 0.02gm/s

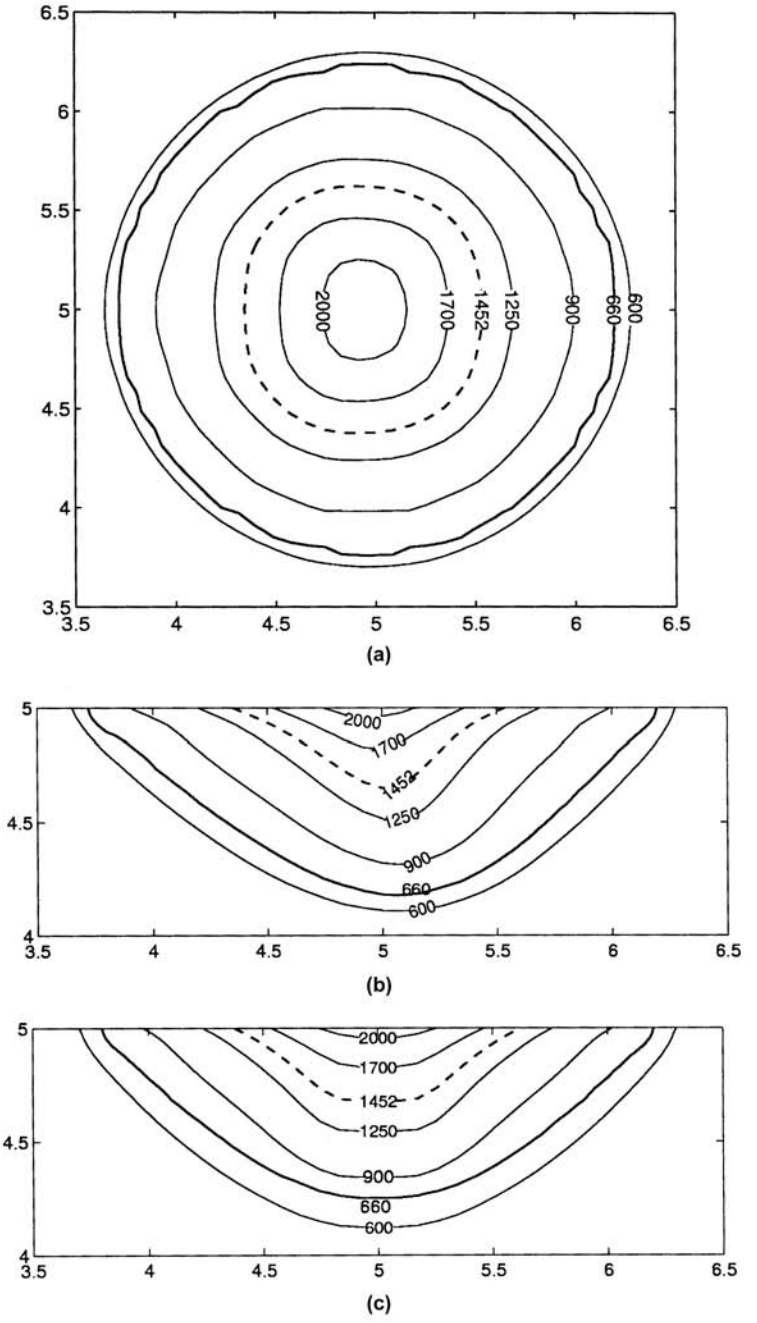

Note: (a) top view, (b) longitudinal sectional view along the laser centre line and (c) cross sectional view in the plane of the laser.
All dimensions are in mm, temperature levels are in degree Centigrade and the contour label 660°C represents the melting temperature of the base metal

Figure 4.
Temperature contours for the case of u_{scan} = 0.008m/s, *power* = 2.4kW, η = 0.22, and *powderfeed* = 0.02gm/s

of laser scanning and latent heat interaction. The particles introduced in the melt pool surface can fall in either region, as shown in Figure 5. It is found in the computation that when the nickel particles fall within the inner cup, where the temperatures are well above the melting point of nickel, they melt very quickly. As a result, they act as species sources at locations where they enter the melt pool surface. If a particle falls between the two cups as shown in Figure 5, it will be first dragged or advected radially outwards by the strong Marangoni convection. Subsequently, as can be seen from Figure 5b, these particles can reach the inner cup and begin to melt. This happens because of the turning effect at the edges of the melt pool (see Figures 3b and 3c). Instantaneously, the molten species diffuses locally, thus acting as a mass source at that location. Hence, instead of having a species mass source only on the surface of the pool, we will now have a species source distributed inside the melt pool. Mathematically, the distributed mass sources act as a species generation term at the corresponding locations. In this manner, the source terms generated due to each and every particle introduced on the surface are calculated and statistical data are maintained for each control volume. These data of species mass source distribution are then used in solving the species conservation equation. Typical surface temperature variation of the particles following the trajectories shown in Figure 5 is depicted in Figure 6.

Solute concentration in the melt pool

The concentration field obtained inside the molten pool with the distributed source terms is shown in Figure 7. In this case, the maximum concentration of nickel is found near the centre of the melt pool surface. The reason for this can be explained as follows. From the concentration field (Figure 7) and the temperature field (Figure 4), it may be noticed that the concentration of the species is more on the top surface of the "inner cup", where the nickel particles are found to melt almost instantaneously. Hence, due to the effect of distributed species mass source, the melt pool always experiences a concentrated species flux on the portion of the pool surface within the inner cup, where the temperature ranges from the melting point of the alloying element to the maximum temperature of the pool (just beneath the laser). The species mass is almost zero in the remaining area of the melt pool surface. This results in a maximum concentration always near the centre of the melt pool surface. However, the effect of dilution and solute rejection also features at the melting and solidification fronts, respectively. This can be visualised by comparing the concentration fields near the solidification front and the melting front, where it is found that the average concentration is more near the solidification front than near the melting front due to solute rejection and dilution, respectively. It is also clear from Figure 7b that the iso-concentration lines are not vertical but stretched towards the solidification front. The final concentration distribution inside the melt pool is determined by the solution of the species conservation equation (29), which includes advection and diffusion in addition to the distribution of species sources described above.

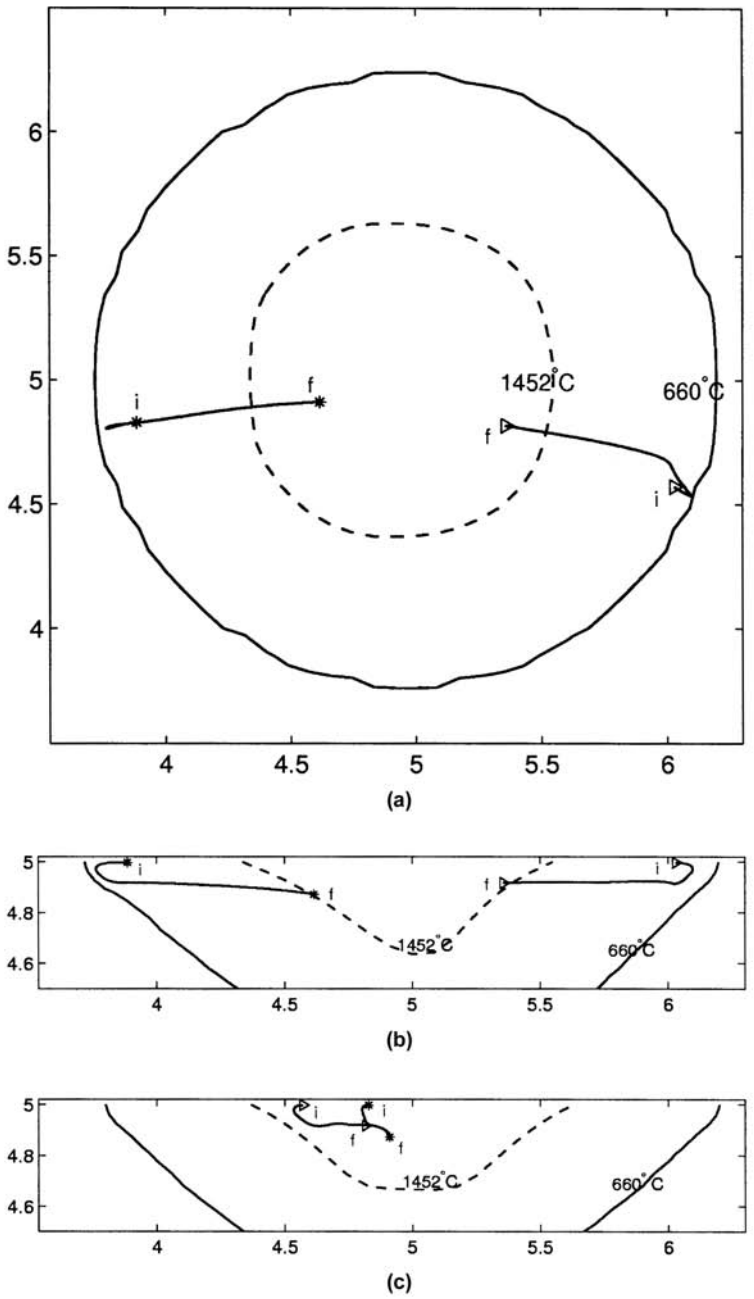

Note: (a) top view, (b) longitudinal sectional view along the laser centre line and (c) cross sectional view in the plane of the laser.
All dimensions are in mm, i and f denote the initial and final locations of the particle. Solid line and dotted line indicates solid-liquid interface (melting of aluminium) and 1452°*C* contour (melting point of nickel), respectively

Figure 5.
Particles' behaviour in the melt pool

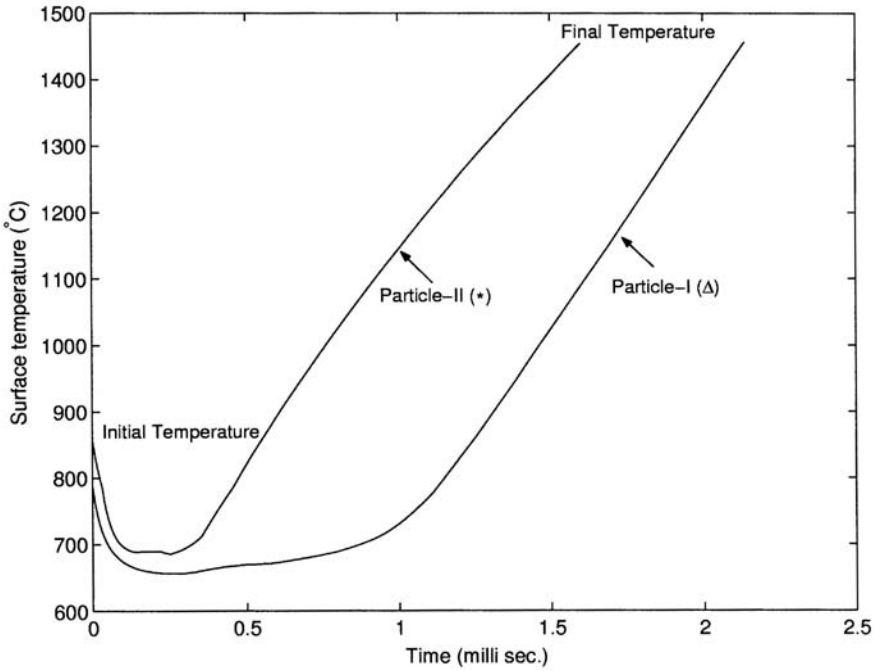

Figure 6.
Surface temperature variation of the particles with time for various locations in the melt pool are shown for particles demonstrated in Figure 5

Solute concentration field of the solidified alloy

The solute concentration distribution in the solidified alloy can be determined from the concentration distribution at the solidification front. Since the solubility of the solute in the solid phase is less than that in the liquid phase, the solute enters the solid phase with a concentration of k_pC. If we multiplied the species concentration at any point on the solidification front by k_p and then map it on a vertical line, we would obtain the concentration variation with height along the centre line of the solidified material (Figure 8a). If the same procedure is repeated for other longitudinal planes away from the centre line, a full mapping of the species concentration distribution in a cross-section of the solidified alloy can be obtained, as shown in Figure 8b. A striking result seen in the interface composition variation shown in Figure 8a-b is that the maximum composition of nickel is found near the bottom of the solidified alloy. The reason for this behaviour can be explained as follows. If the concentration field is viewed at the longitudinal section of the molten pool (shown in Figure 7b), it may be observed that the iso-concentration lines near the bottom are shifted towards the solidification front due to the effect of convection and distributed species source terms. Hence, during solidification, the bottom portion of the solidification front will experience more concentration. After multiplying the concentration at any location at the solidification interface with the partition coefficient, we will obtain the corresponding concentration at that location in the solidified alloy. In the cross-sectional view of the solidified alloy concentration distribution (Figure 8b), we can see that the concentration is

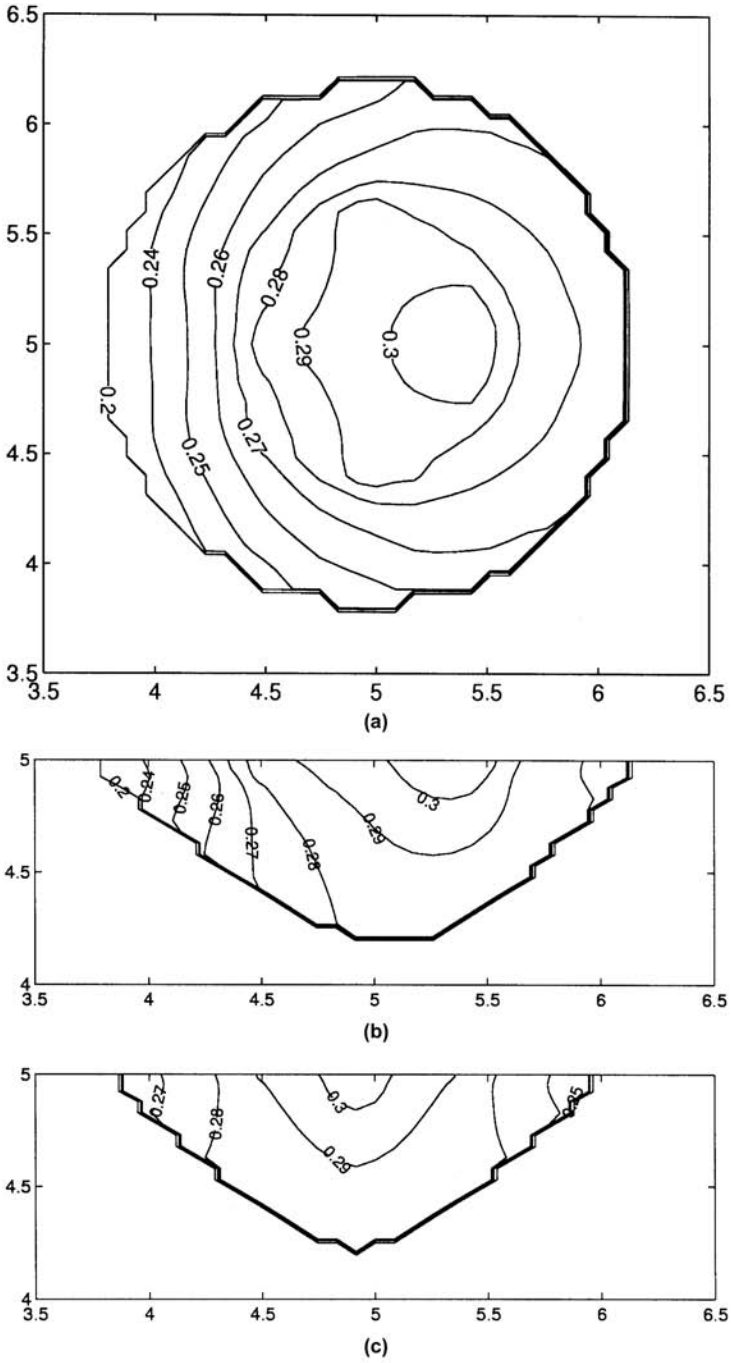

Note: (a) top view, (b) longitudinal sectional view along the laser centre line and (c) cross sectional view in the plane of the laser.
All dimensions are in mm

Figure 7.
Solute concentration field in the molten pool (in terms of mass fraction of nickel) for the case of u_{scan} = 0.008m/s, *power* = 2.4kW, η = 0.22, and *powderfeed* = 0.02gm/s

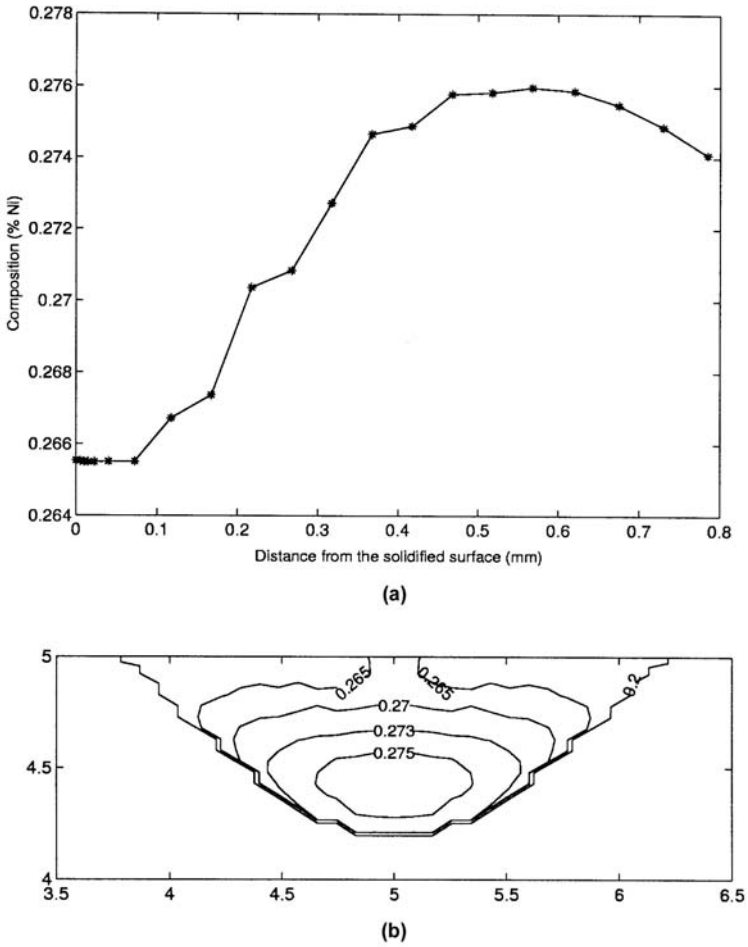

Note: (a) concentration variation with height along the solidification interface in a longitudianl plane along the laser centreline (b) concentration field in a cross section of solidfied alloy. All dimensions are in mm

Figure 8.
Solute concentration field in the solidified alloy (in terms of mass fraction of nickel) for the case of u_{scan} = 0.008m/s, *power* = 2.4kW, η = 0.22, and *powderfeed* = 0.02gm/s

found to increase towards the centre of the solidified alloy cross-section. This can be explained from the cross-sectional view of the temperature field (Figure 4c). The region bounded by the inner cup is comparatively smaller than the total cross-section of the melt pool. Hence, the distributed mass source is concentrated within the inner cup, resulting in a concentrated species source near the centre of the melt pool. Thus, we may expect more concentration of species near the middle of the solidified alloy.

Using the same parameters for Ni on Al, a comparison is made between the present case (i.e. distributed melting case) and the case performed with the species added entirely as a flux condition at the pool surface (according to equations (36) and (37)). The results obtained are compared for the interface

composition variation with height, which is shown in Figure 9. There is a significant difference found between the two results, which further confirms that for relatively higher melting point alloying elements, the distributed melting approach has to be adopted in order to predict a more realistic composition distribution. The numerical results shown in Figure 9 also show a comparison with the experimental findings of Balachandran (1998), and it is found that the experimental trend is more accurately captured by the present model than by the one without source term modification.

Conclusions

A three-dimensional transient numerical model is developed to predict the mass, momentum, heat and species transport during LSA. The addition of alloying element to the molten pool is represented by formulation of a species source term in the solute transport equation. To achieve this purpose, the alloyed particles are tracked in the melt pool. Simultaneously, the temperature distribution inside the spherical particles is solved by assuming its surface temperature to be the local temperature in the melt pool. The amount of particle mass that fuses as it passes through a particular control volume is used as a species mass source to solve the species conservation equation. Numerical computations are performed for Ni as an alloying element on Al base metal. It is found that the present model represents the actual species in a more realistic manner than a model without provision for representing distributed melting situations.

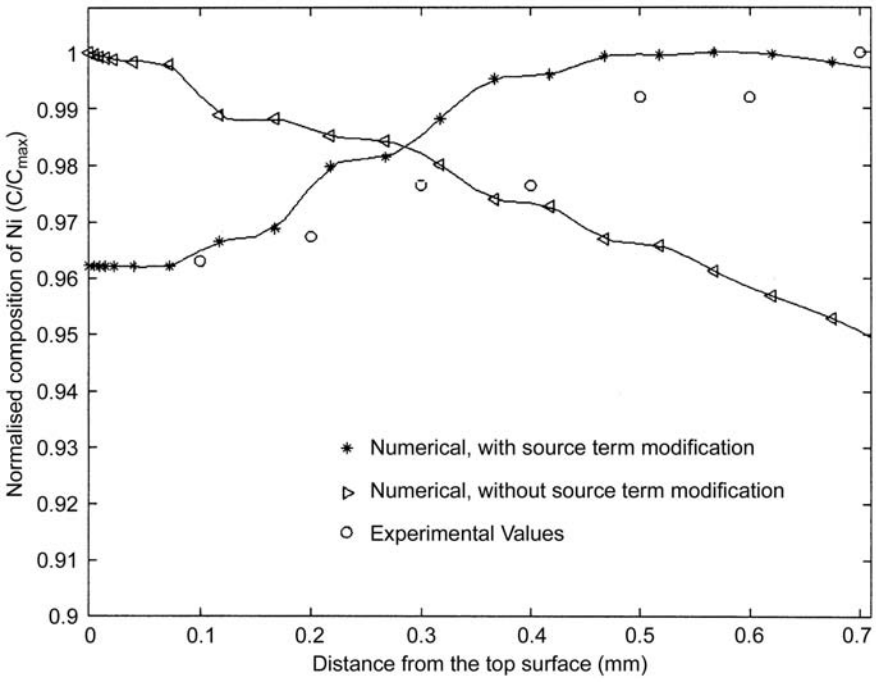

Figure 9.
Comparison of numerical and experimental results for the solidified interface composition with the same parameters

References

Balachandran, R. (1998), "Laser surface alloying of nickel on aluminium substrate", ME thesis, Indian Institute of Science, Department of Metallurgy, Bangalore

Basu, B. and Srinivasan, J. (1988), "Numerical study of steady state laser melting problem", *Int. J. Heat Mass Transfer*, Vol. 11, pp. 2331-8.

Brandes, E.A. (1983), *Smithels Metals Reference Book*, Butterworth and Co. Ltd, London.

Brent, A.D., Voller, V.R. and Reid, K.J. (1988), "Enthalpy-porosity technique for modelling convection-diffusion phase change: application to the melting of a pure metal", *Numer. Heat Transfer A*, Vol. 13, pp. 297-318.

Carslaw, H.S. and Jaeger, J.C. (1959), *Conduction of Heat in Solids*, Oxford University Press, Oxford.

Chan, C.L., Mazumdar, J. and Chen, M.M. (1984), "Two dimensional transient model for convection in laser melted pool", *Metall. Trans. A*, Vol. 15A, pp. 2175-84.

Chan, C.L., Mazumdar, J. and Chen, M.M. (1987), "Three dimensional axisymmetric model for convection in laser melted pools", *Materials Science and Technology*, Vol. 3, pp. 306-11.

Chan, C.L., Mazumdar, J. and Chen, M.M. (1988), "Effect of surface tension gradient driven convection in a laser melt pool: three dimensional perturbation model", *Journal of Applied Physics*, Vol. 64 No. 11, pp. 6166-75.

Chen, J.C. and Huang, Y.C. (1990), "Thermocapillary flow of surface melting due to a moving heat flux", *Int. J. Heat Mass Transfer*, Vol. 34 No. 3, pp. 663-71.

Dutta, P., Joshi, J. and Janaswami, R. (1995), "Thermal modeling of GTAW process with non axisymmetric boundary conditions", *Numer. Heat Transfer A*, Vol. 27, pp. 499-518.

He, X., Mordike, B.L., Pirch, N. and Kreutz, E.W. (1995), "Laser surface alloying of metallic materials", *Lasers in Engineering*, Vol. 4, pp. 291-316.

Kou, S. and Wang, Y.H. (1986), "Three dimensional convection in laser melted pools", *Metall. Trans. A*, Vol. 17A, pp. 2265-70.

Patankar, S.V. (1980), *Numerical Heat Transfer and Fluid Flow*, Hemisphere, New York, NY.

Sarkar, S., Chakraborty, S. and Dutta, P. (2001), "A scaling analysis of momentum and heat transport in laser surface melting", *Lasers in Engineering* (in press)

Voller, V.R. and Prakash, C. (1987), "A fixed grid numerical modeling methodology for convection/diffusion phase change problems", *Int. J. Heat Mass Transfer*, Vol. 30, pp. 1709-19.